



Title	Predictability of the Barents Sea Ice in Early Winter: Remote Effects of Oceanic and Atmospheric Thermal Conditions from the North Atlantic
Author(s)	Nakanowatari, Takuya; Sato, Kazutoshi; Inoue, Jun
Citation	Journal of Climate, 27(23), 8884-8901 https://doi.org/10.1175/JCLI-D-14-00125.1
Issue Date	2014-12-01
Doc URL	http://hdl.handle.net/2115/59468
Rights	© Copyright 2014 American Meteorological Society (AMS). Permission to use figures, tables, and brief excerpts from this work in scientific and educational works is hereby granted provided that the source is acknowledged. Any use of material in this work that is determined to be "fair use" under Section 107 of the U.S. Copyright Act or that satisfies the conditions specified in Section 108 of the U.S. Copyright Act (17 USC § 108, as revised by P.L. 94-553) does not require the AMS' s permission. Republication, systematic reproduction, posting in electronic form, such as on a web site or in a searchable database, or other uses of this material, except as exempted by the above statement, requires written permission or a license from the AMS. Additional details are provided in the AMS Copyright Policy, available on the AMS Web site located at (http://www.ametsoc.org/) or from the AMS at 617-227-2425 or copyright@ametsoc.org .
Type	article
File Information	jcli-d-14-00125.1(2).pdf



[Instructions for use](#)

Predictability of the Barents Sea Ice in Early Winter: Remote Effects of Oceanic and Atmospheric Thermal Conditions from the North Atlantic

TAKUYA NAKANOWATARI

Institute of Low Temperature Science, Hokkaido University, Sapporo, Japan

KAZUTOSHI SATO

The Graduate University for Advanced Studies, Tachikawa, and Research and Development Center for Global Change, JAMSTEC, Yokosuka, Japan

JUN INOUE

The Graduate University for Advanced Studies, Tachikawa, Research and Development Center for Global Change, JAMSTEC, Yokosuka, and National Institute of Polar Research, Tachikawa, Japan

(Manuscript received 11 February 2014, in final form 4 September 2014)

ABSTRACT

Predictability of sea ice concentrations (SICs) in the Barents Sea in early winter (November–December) is studied using canonical correlation analysis with atmospheric and ocean anomalies from the NCEP Climate Forecast System Reanalysis (CFSR) data. It is found that the highest prediction skill for a single-predictor model is obtained from the 13-month lead subsurface temperature at 200-m depth (T200) and the in-phase meridional surface wind (V_{sfc}). T200 skillfully predicts SIC variability in 35% of the Barents Sea, mainly in the eastern side. The T200 for negative sea ice anomalies exhibits warm anomalies in the subsurface ocean temperature downstream of the Norwegian Atlantic Slope Current (NwASC) on a decadal time scale. The diagnostic analysis of NCEP CFSR data suggests that the subsurface temperature anomaly stored below the thermocline during summer reemerges in late autumn by atmospheric cooling and affects the sea ice. The subsurface temperature anomaly of the NwASC is advected from the North Atlantic subpolar gyre over ~ 3 years. Also, V_{sfc} skillfully predicts SIC variability in 32% of the Barents Sea, mainly in the western side. The V_{sfc} for the negative sea ice anomalies exhibits southerly wind anomalies; V_{sfc} is related to the large-scale atmospheric circulation patterns from the subtropical North Atlantic to the Eurasian continent. This study suggests that both atmospheric and oceanic remote effects have a potential impact on the forecasting accuracy of SIC.

1. Introduction

The Barents Sea is a transition zone for warm and saline waters on their way from the Atlantic to the Arctic Ocean (Fig. 1). The major current, the Norwegian Atlantic Current, is a poleward extension of the Gulf Stream and the North Atlantic Current (Polyakov et al. 2005). The North Atlantic Current splits into two branches in the eastern North Atlantic. The eastern branch, known as the Norwegian Atlantic Slope Current (NwASC), is an

approximately 3500-km-long nearly barotropic shelf edge current flowing along the Norwegian shelf break that tends to flow into the Barents Sea and Arctic Ocean.

A number of studies have analyzed observational datasets and historical ice observations showing that the Barents Sea is one of the Arctic regions with the largest sea ice variability on different time scales (Deser et al. 2000; Vinje 2001; Divine and Dick 2006). Because air–sea temperature differences in the Barents Sea are extremely large, ocean heat release reaches values of 300–500 W m^{-2} (Simonsen and Haugan 1996). The Barents Sea dominates the seasonal Arctic heat budget and has the most vigorous ocean–air exchange in the Arctic, making it a “hot spot” of influence on the high-latitude climate system (Serreze et al. 2007). The role of the

Corresponding author address: Takuya Nakanowatari, Japan Agency for Marine–Earth Science and Technology, 2-15 Natsumishima-cho, Yokosuka, 237-0061, Japan.
E-mail: nakanow@jamstec.go.jp

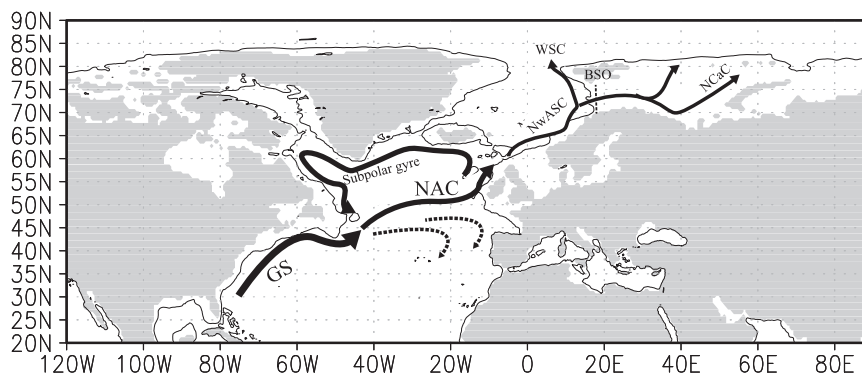


FIG. 1. Schematic of ocean currents and geographic locations. Black arrows represent the Gulf Stream (GS), North Atlantic Current (NAC), subpolar gyre, Norwegian Atlantic Slope Current (NwASC), North Cape Current (NCaC), and West Spitsbergen Current (WSC). The Barents Sea Opening (BSO) is shown by a dashed line. The branching of the GS is shown by dashed arrows. The contour level is 500-m depth.

Barents Sea in the Arctic climate system is reviewed by [Smedsrud et al. \(2013\)](#).

In contrast to the warming occurring in the summer over the Arctic region, the Eurasian continent has recently experienced severe winters ([Petoukhov and Semenov 2010](#); [Peings and Magnusdottir 2014](#); [Vihma 2014](#); [Screen 2014](#); [Screen and Simmonds 2014](#); [Cohen et al. 2014](#)) and the frequency of extreme weather events has increased in the midlatitudes ([Francis and Vavrus 2012](#)). According to climate change experiments based on phase 5 of the Climate Model Intercomparison Project (CMIP5), this cold Eurasia/warm Arctic anomaly will continue in the future ([Yang and Christensen 2012](#)). [Honda et al. \(2009\)](#) suggested that the severe wintertime climate over Eurasia is related to a dynamic atmospheric response through the modification of a stationary Rossby wave generated thermally through anomalous turbulent heat fluxes in the Barents and Kara Seas from late autumn to early winter. [Inoue et al. \(2012\)](#) showed that the decrease in sea ice area over the Barents Sea in early winter also affects cyclonic pathways in the downstream region and results in the cold Eurasia/warm Arctic pattern. The Barents Sea ice extent in winter has decreased since 1850 ([Shapiro et al. 2003](#)), and the retreat observed during recent decades has been the largest decrease in the Arctic ([Parkinson and Cavalieri 2008](#)). Along with the recent sea ice decrease, abnormally cold winters have also frequently occurred in far eastern Eurasia in recent years (2005/06, 2011/12, 2012/13). Thus, understanding the mechanism of the wintertime sea ice variability in the Barents Sea may be of great importance for the improvement of wintertime climate forecasting for Eurasia.

Variations in the Barents Sea ice have been attributed to a number of processes, including large-scale atmospheric

circulation anomalies ([Maslanik et al. 2007](#); [Deser and Teng 2008](#); [Zhang et al. 2008](#)), cyclone activity ([Sorteberg and Kvingedal 2006](#); [Simmonds and Keay 2009](#)), local winds and ice import from the Arctic Ocean ([Hilmer et al. 1998](#); [Koenigk et al. 2009](#); [Kwok 2009](#)), and oceanic heat anomalies generated locally ([Schlichtholz 2011](#)) or advected into the Barents Sea ([Vinje 2001](#); [Kauker et al. 2003](#); [Francis and Hunter 2007](#)). Numerical simulations demonstrate that the interannual variability and longer-term decrease in the sea ice area reflect the variability of the Atlantic inflow ([Årthun and Schrum 2010](#); [Sandø et al. 2010](#); [Årthun et al. 2012](#); [Koenigk and Brodeau 2014](#)). Recently, [Schlichtholz \(2013\)](#) pointed out based on observational data that the wintertime (December–March) surface air temperature and sea ice variability is to a large extent driven by anomalous local meridional winds. However, the remote effects of the atmospheric and oceanic heat conditions on the changes in the Barents Sea ice have not yet been fully examined because of the limited spatial coverage of oceanographic data and models.

Over the past few years, a new generation of atmosphere–ocean coupled reanalysis, the National Centers for Environmental Prediction Climate Forecast System Reanalysis (NCEP CFSR), has been produced. The NCEP CFSR has benefited from advances in operational weather forecasting and previous reanalysis improvements ([Bengtsson et al. 2007](#)). The NCEP CFSR assimilates the oceanic field including sea ice concentration (SIC). Therefore, it is expected that the predictability of the sea ice and its relation to the atmosphere and ocean variability can be examined.

In this study, we identify the appropriate variables for the seasonal forecasting of the Barents Sea ice in

winter based on the NCEP CFSR data. It has been suggested that the surface heat fluxes in the Barents Sea are relatively large in the beginning of winter and thus seem to be essential for the following severe winter in Eurasia (e.g., Inoue et al. 2012). We therefore mainly focus on the predictability of the interannual variability of the Barents Sea ice in early winter (November–December). Canonical correlation analysis (CCA) is used both as a forecasting and a diagnostic tool to explore potential dynamic pathways in the climate system that link variability in atmospheric and oceanic predictors to variability in sea ice. For the oceanic predictor, we focus on the remote effects of the subsurface ocean temperature anomaly in the North Atlantic on the ocean heat conditions. The datasets and methodology are presented in section 2, where we show the representation of the interannual variability of the sea ice and the ocean thermal condition of the NCEP CFSR data. In section 3 we present results from each predictor experiment, and section 4 closes the paper with a summary and discussion.

2. Data and methods

a. Data

The monthly means of SIC and atmosphere–ocean data used for the CCA are derived from a coupled global NCEP CFSR dataset from 1979 to 2009 (Saha et al. 2010). The NCEP CFSR was designed and executed as a global, high-resolution, coupled atmosphere–ocean–land surface–sea ice system to provide the best estimate of the state of these coupled domains over this period. The global atmospheric resolution of the NCEP CFSR is ~ 38 km (T382) with 64 levels. The spatial resolution of the global ocean is 0.25° at the equator, extending to 0.5° beyond the tropics, with 40 levels (11 layers from the uppermost level of 5-m to 105-m depth). Two daily SST analyses based on Advanced Very High Resolution Radiometer (AVHRR) and Advanced Microwave Scanning Radiometer (AMSR) satellite data from November 1981 are assimilated in the NCEP CFSR data, and thus the interannual variation of SST is close to the observations. Conversely, for the region below the surface, the ocean temperature variability is likely to be highly dependent on the ocean model because the number of ocean temperature measurements by XBT, mainly derived from the World Ocean Database 1998 (Conkright et al. 1999) and Argo floats (Roemmich et al. 2001), is fairly small north of 65°N . The salinity data are not directly assimilated in the NCEP CFSR data, whereas several data sources, such as the global ice concentration data from the Goddard Space Flight Center (Cavalieri 1994;

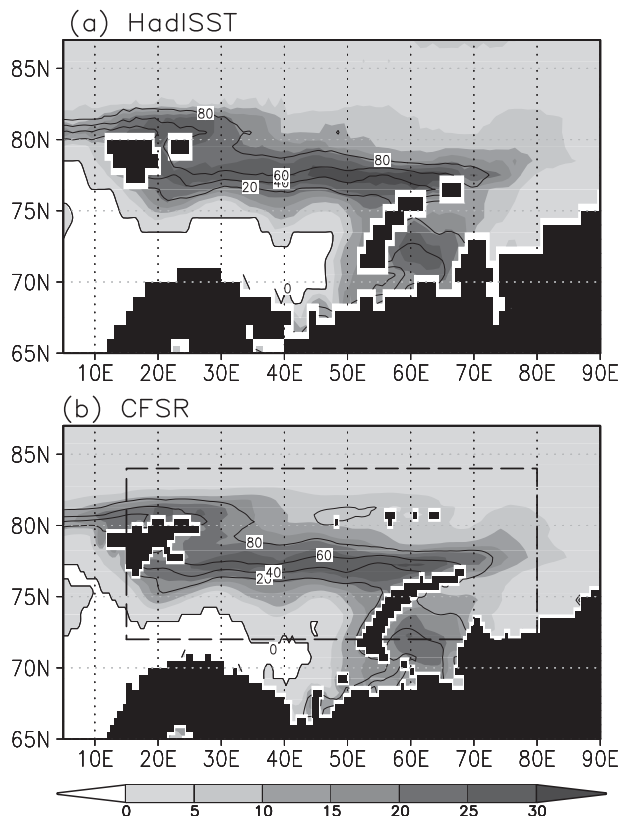


FIG. 2. Sea ice concentration (% in contours) and its standard deviation (shading) in November–December from the (a) HadISST and (b) NCEP CFSR data. The rectangle (72° – 84°N , 15° – 80°E) indicates the region of the predictand for the canonical correlation analysis (CCA).

Cavalieri et al. 1996) and the NCEP operational ice analysis (Grumbine 1996), are assimilated for the SIC. In the Northern Hemisphere, the NCEP CFSR sea ice extent in September shows interannual fluctuations similar to those in data from the National Snow and Ice Data Center, although the former has greater bias than the latter starting in 1997 (Wang et al. 2011).

We used the monthly mean SIC data from November–December to represent Barents Sea ice in early winter. To evaluate the representation of the Barents Sea ice in early winter, we used SIC data derived from the Hadley Centre Sea Ice and Sea Surface Temperature dataset version 1 (HadISST; Rayner et al. 2003) on a $1^\circ \times 1^\circ$ latitude/longitude grid. Figures 2a and 2b show the climatological SIC and the standard deviation of the SIC anomalies in November–December from the HadISST and NCEP CFSR, respectively. The location of the sea ice edge in the NCEP CFSR data is very similar to that in the observations, although the standard deviation of the SIC in the NCEP CFSR data is relatively low. The NCEP CFSR also successfully tracks the temporal variability of

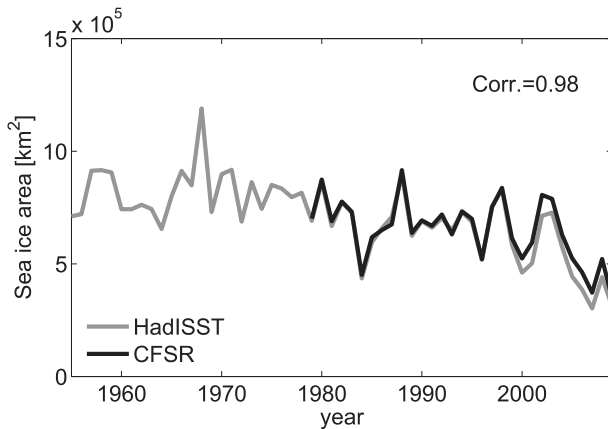


FIG. 3. Time series of the sea ice area in November–December averaged over the Barents Sea (70° – 82° N, 15° – 70° E), derived from the HadISST (gray) and NCEP CFSR data (black).

the sea ice area within the Barents Sea (70° – 82° N, 15° – 70° E) when compared with HadISST ($r = 0.98$; Fig. 3). Even if we remove the linear trend from both time series by regression analysis, the correlation between them is still high ($r = 0.85$). This match of the temporal variability of the NCEP CFSR supports the idea that these reanalysis data can be used to examine the interannual variability of the SIC in the Barents Sea and its cause.

It has been reported that the dominant modes of upper ocean heat content variability associated with El Niño–Southern Oscillation, the Indian Ocean dipole, the Pacific decadal oscillation, and the Atlantic meridional overturning circulation are well represented in the NCEP CFSR (Xue et al. 2011). However, these modes are intrinsic in the tropics, and the representation of ocean variability in the polar region has not yet been examined. We therefore evaluated the representation of the oceanic components in the NCEP CFSR data by comparing them with independent observations, which are not assimilated in the NCEP CFSR data.

For ocean temperature, we used the monthly mean subsurface temperature data from the Kola section. High-quality data are available from the Polar Research Institute of Marine Fisheries and Oceanography (PINRO), Murmansk, Russia, from 1951 onward for this section (along 33.5° E from 70° to 75° N; Fig. 4) that crosses the Atlantic water inflow in the Barents Sea. Observations are recorded on a monthly basis (Hughes et al. 2009) for the entire water column where depth varies from 0 to 200 m. We used the monthly mean averaged from 50 to 200 m at stations 1–3 of the Kola section (70° – 72° N; Fig. 4), which approximately corresponds to the current axis of the North Cape Current (NCaC; Fig. 1). We also used the ocean temperature data along the Barents Sea Opening (BSO; Fig. 1), which are monitored by the

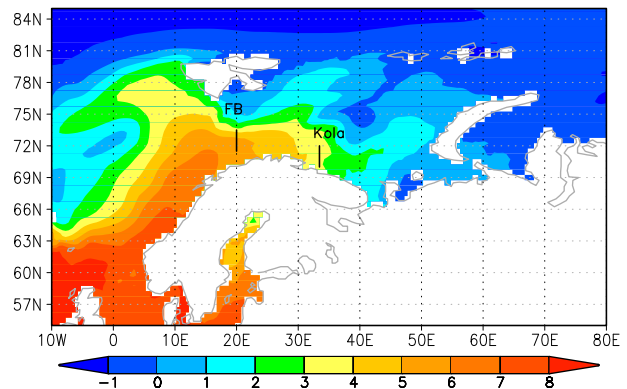


FIG. 4. Annual mean of subsurface (45–205-m depth) potential temperature from the NCEP CFSR data. The thick line indicates the Kola (70° – 72° N) and FB (71.5° – 73.5° N) sections.

Norwegian Hydrographic Service. The data from the BSO are compiled and provided by the Institute of Marine Research, Norway (Blindheim and Loeng 1981). We used the annual mean averaged from 50 to 200 m at the Fugloya–Bear Island (FB) section (71.5° – 73.5° N; Fig. 4).

Next, we evaluated the interannual variability of the NCEP CFSR ocean thermal condition in the Barents Sea. Because the core of the Atlantic water inflow corresponds approximately to the depth from 100 to 300 m (Schlichtholz and Houssais 2011), we examined the subsurface temperature averaged from 50 to 200 m for the index of the Atlantic water temperature. Figure 4 shows the climatology of the subsurface temperature from the NCEP CFSR data. A relatively warm water tongue is evident along the NCaC (Fig. 1), indicating that the advective heat fluxes associated with this ocean current are well represented. The annual mean of the volume transport across the BSO (Fig. 1) calculated from the NCEP CFSR data is ≈ 2 Sv, which is comparable to that from the mooring observation (1.8 Sv) (Skagseth et al. 2008).

The time series of observed and NCEP CFSR monthly mean temperature anomalies in the Kola section show long-term variability with a cycle of several decades (Fig. 5a). The correlation between these time series is 0.80 from 1979 to 2008. The linear trend of the NCEP CFSR temperature anomalies is $0.33^{\circ}\text{C decade}^{-1}$, which is comparable to the observed trend ($0.46^{\circ}\text{C decade}^{-1}$). These results indicate that the NCEP CFSR quantitatively captures the interannual variability and trend of the subsurface temperature in the Barents Sea. The NCEP CFSR subsurface temperature in the FB section is also highly correlated with the observed data on an interannual time scale ($r = 0.92$) (Fig. 5b). The correlation between the detrended subsurface temperature anomalies is 0.69. These comparisons also support the idea that

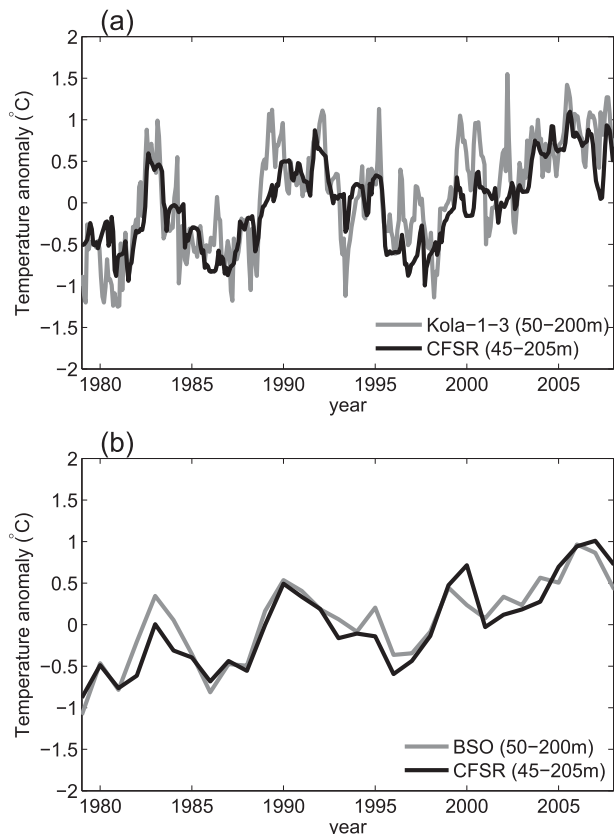


FIG. 5. (a) Time series of the monthly mean of potential temperature anomalies averaged from 50- to 200-m depth along the Kola section (70° – 72.5° N, 33.5° E; gray) and NCEP CFSR data (black). (b) Time series of the annual mean of potential temperature anomalies averaged from 50- to 200-m depth along the BSO (71.5° – 73.5° N, 20° E; gray) and NCEP CFSR data (black).

the interannual variation of ocean temperature in the Barents Sea is successfully represented in the NCEP CFSR. Conversely, the climatological subsurface temperature in the NCEP CFSR is 3.4°C for the Kola and 4.6°C for the FB sections, which are approximately 0.5° – 1.0°C cooler than the observed data in each section. This may be related to that the spatial resolution of the ocean model is insufficient to represent the narrow structure of the NwASC and NCaC.

b. Predictand and predictors

The predictand is the November–December average SIC from 1980 to 2009 in the Barents Sea. The observed climatological SIC (Fig. 2a) shows that the interannual variability is prominent along the ice edge and relatively large in the offshore region of Novaya Zemlya, and the southern part of the Barents Sea is not covered with sea ice. In the area around Frans Josef Land, the SIC is close to 100%. Therefore, the analyzed area is bounded by 72° – 84° N, 15° – 80° E (Fig. 2b), which covers the region

where the interannual variability is high. Grid cells where the SIC is zero during the entire analysis period were not used. The winter anomaly time series at each grid cell was constructed by removing the 1980–2009 mean from each early winter.

Seven climate variables were tested as potential predictors: 2-month-averaged SST, subsurface temperature, surface air temperature (SAT), zonal (U_{sfc}) and meridional (V_{sfc}) wind, sea level pressure (SLP), and geopotential height at 500 hPa ($z500$). The local SST is known to be a good indicator of the predictand for sea ice in the Barents Sea (Schlichtholz 2011). The subsurface temperature in the BSO is closely related to the ocean heat transport from the Atlantic Ocean rather than the SST. We adopted the potential temperature at 200-m depth (T200) as the subsurface temperature because the Atlantic water inflow into the Barents Sea has a core between 100- and 300-m depth (Schlichtholz and Houssais 2011). To examine the effects of the ocean thermal anomaly from the North Atlantic, the areas analyzed for these local predictors are extended meridionally and zonally (60° – 90° N, 0° – 80° E), compared with the area for the SIC. Because the interannual variability of wintertime sea ice extent in the Barents Sea is known to be considerably influenced by simultaneous local wind anomalies (Sorteberg and Kvingedal 2006), we also examined the effects of local SAT and zonal (U_{sfc}) and meridional wind (V_{sfc}). Northern Hemisphere SLP and $z500$ are included because the preferred modes of low-frequency atmospheric variability and teleconnection patterns have been previously identified for these variables (e.g., Wallace and Gutzler 1981).

c. Canonical correlation analysis methodology

CCA is a multivariate statistical technique that measures the linear relationship between two or more multidimensional variables. The objective of CCA is to find correlated patterns and lead–lag relationships between the predictor and predictand fields. The end result of CCA is a series of modes where each mode is a pair of predictor and predictand patterns (canonical component vectors), each with a time series (canonical component time series) that describes how each pattern varies in time. The technique is slightly different from the more commonly used singular value decomposition because the cross-correlation, instead of maximizing covariance, is maximized (von Storch and Zwiers 1999). In climate research, CCA is used to identify coupled patterns in climate data (Bretherton et al. 1992). A variant of CCA, developed by Barnett and Preisendorfer (1987), is the most reliable and commonly used statistical seasonal forecasting technique (Zwiers and von Storch 2004). The CCA technique has also been

used to examine the seasonal forecast skill for July SIC variability in Hudson Bay (Tivy et al. 2011).

The general CCA methodology applied in this study follows Barnett and Preisendorfer (1987). The predictor and predictand data are standardized and prefiltered using principal component (PC) analysis. The PCs are truncated to reduce the amount of noise in the predictor and predictand datasets prior to CCA. The choice of PC truncation points in this study was determined using Monte Carlo techniques (100 trials) (Barnett and Preisendorfer 1987). The truncation rules for the CCA are the same as those for PC. This usually results in four to six canonical modes.

Models were generated for each predictor at lead times from 0 to 16 months with 2-month averages for each predictor. Because the sea ice area in November–December is affected by the integration of the preceding atmospheric and oceanic forcings, we used the 2-month averages for the predictors. To determine whether sources of skill identified in the single-predictor experiments were unique to a specific predictor field or common to two or more predictor fields, mixed predictor experiments were run. We assumed that if the skill of the mixed predictor experiment is higher than the skill of the individual predictor experiment, the signals are unique. Livezey and Smith (1999) pointed out that the PC modes determined by the Monte Carlo techniques are too small. This problem seems to be crucial for mixed predictor experiments, because the mixed predictor field includes a large number of PC modes rather than each field. We therefore applied the methodology of O’Lenic and Livezey (1988), where the truncation point is determined by screen plots to calculate the PC modes in the mixed predictor experiments.

The forecast skill for each predictor was evaluated by the field-averaged cross-validated correlation (FCC) between the observed and modeled data. FCC is the standard metric used in the literature to evaluate the skill of CCA-based forecasting models (e.g., Barnston 1994). That is, each of the 29 years from 1980 to 2009 is excluded in turn, and the remaining 28 years are used for CCA. The entire sequence of CCA procedure is performed for each case to obtain the predicted SIC in the entire analyzed period. FCC is calculated by averaging the correlation between the observed and predicted SIC in each grid point over the analyzed area. This cross-validation scheme is commonly used to prevent overfitting of the statistical prediction model (Michaelsen 1987; Elsner and Schmertmann 1994).

The significance of local skill (skill at a single grid point) is determined with a Monte Carlo simulation using a phase randomization technique generating 1000 surrogate time series (Kaplan and Glass 1995). First,

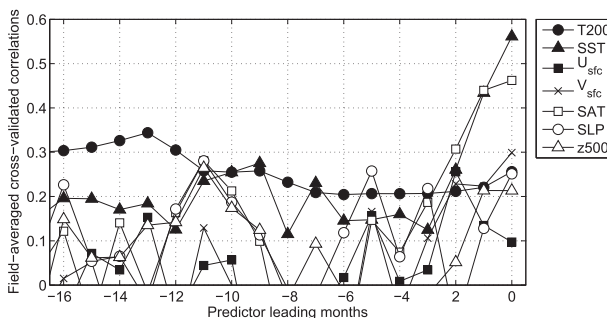


FIG. 6. Forecast skill (field-averaged cross-validated correlation) for 0-month (November–December) to 16-month (July–August) lead from local T200, SST, zonal wind (U_{sfc}), meridional wind (V_{sfc}), SAT, Northern Hemisphere SLP, and z500.

absolute Fourier amplitudes (square root of spectra) for the observed SICs are estimated in each grid point, and then 1000 surrogate time series are generated by an inverse Fourier transform with the observed Fourier amplitudes and randomized phases. Surrogate correlation coefficients are estimated between the surrogate and observed SIC time series. The relative position of the absolute value of the observed correlation coefficients in the sorted absolute values of the surrogate correlation coefficients gives the level of confidence for the observed correlation coefficient in each grid point. Because this method takes into account the spectrum structure of the time series, it is more conservative than the significance test based on the t test.

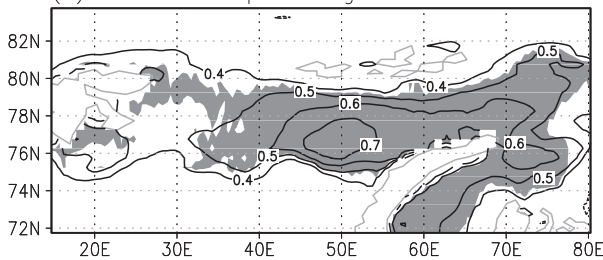
3. Results

a. Forecast skill

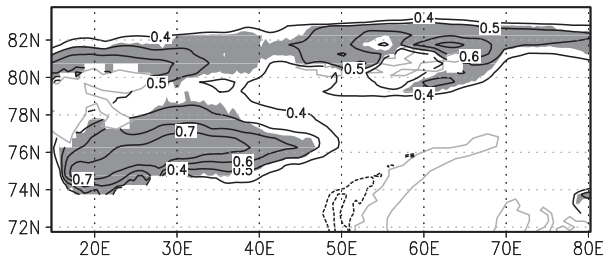
The results from the single-predictor experiments run from 0- to 16-month lead times, predicting November–December SIC, are summarized in Fig. 6. The highest forecast skill (FCC = 0.34) occurred for T200 at a 13-month lead time, except for the SST and SAT at a 0- to 1-month lead time. Figure 7a shows the geographical distribution of the CCA skill for T200. T200 has a significant skill with a cross-validated correlation greater than 0.7 in the eastern Barents Sea, covering 35% of the analyzed area. The forecast skill for T200 reduces from spring to summer (10- to 6-month lead time); however, the forecast skill for SST increases from autumn (2-month lead time) to early winter (0-month lead time). The physical processes that control this lead–lag relationship between the SIC and T200 are explored in the next section.

Meaningful peaks of forecast skill for SST and SLP are found at 9- and 11-month lead times. The peak of the SST is consistent with that of Schlichtholz (2011), who

Cross validated corr. for sic in Nov.–Dec.
(a) T200 in the preceding Oct.–Nov.



(b) Meridional wind in Nov.–Dec.



(c) Mixed

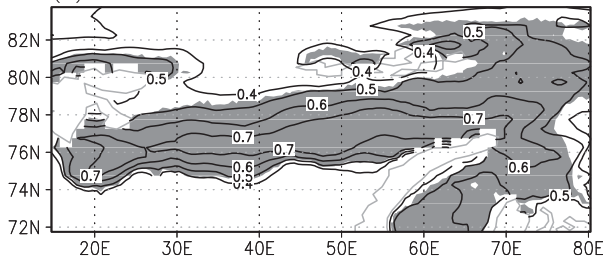


FIG. 7. Geographic distribution of CCA skill (cross-validated correlation) for (a) 13-month lead forecasts from T200, (b) no-time lag forecasts from V_{sfc} , and (c) mixed T200 and V_{sfc} . Shading indicates the region where the cross-validated correlation is significant at the 95% confidence level.

showed that the variability of spring SST near the Barents Sea ice edge explains approximately 66% of the variance of the following winter sea ice area. They suggest that the winter sea ice area is mainly controlled by the postsummer surface reemergence of oceanic heat anomalies generated by earlier atmospheric forcing. In fact, the forecast skill for SAT shows the maximum peak at an 11-month lead time. However, the skill scores for the SST and SAT are less than those for T200 at a 13-month lead time. This implies that the skill score for the T200 appears to be essentially different from the earlier atmospheric forcing. Thus, T200 exhibits higher predictive skill at a 13-month lead time than SST at a 9-month lead time, and the lead time of the former is up to 4 months longer than the latter.

It is interesting to note that the highest forecast skills for V_{sfc} (FCC = 0.30) and SAT (FCC = 0.46) are found at a 0-month lead time (November–December). Because V_{sfc} is not largely affected by the existence of sea ice, high

forecast skill is not apparent. The geographical distribution of skill for V_{sfc} (Fig. 7b) shows that the significant forecast skill is found over the western part of the Barents Sea, covering 32% of the analyzed area. These results are consistent with an earlier study based on observational data (Schlichtholz 2013).

Because T200 and V_{sfc} skillfully predicted the SIC in the eastern and western Barents Sea, respectively, a mixed predictor experiment was conducted using the 13-month lead T200 and in-phase V_{sfc} . The number of PC modes retained in this experiment is 10, which is greater than that determined by the Monte Carlo techniques. The addition of V_{sfc} to the T200 forecasts raised the forecast skill from 0.34 to 0.45 (the coverage of significant forecast skill from 35% to 53%). The geographical distribution of skill for the mixed predictors (Fig. 7c) shows a significant cross-validated correlation skill greater than 0.7 in the eastern and western Barents Sea. The geographic distribution of the forecast skill for the mixed predictor compared with the single-predictor model highlights the fact that each predictor provides unique predictive information and the best model is the combination of the two predictors. We conducted mixed predictor experiments by adding 9-month lead SST and 2-month and 11-month SAT, which have relatively high forecast skill (Fig. 6), to the 13-month lead T200. However these forecast skills are 0.30, 0.34, and 0.40, respectively, which are less than the forecast skill of the mixed T200 and V_{sfc} (0.45). We therefore conclude that the 13-month lead T200 and in-phase V_{sfc} constitute the best combination of all possible mixed predictor experiments for the Barents Sea ice in early winter.

b. Source of predictability

The above evaluation of the forecast skill clarifies that the best match forecast model was a combination of two predictors: T200 (preceding October–November) and V_{sfc} (November–December). In this section, canonical correlation maps and time series are used to explore the sources of predictive skill for each predictor. Table 1 summarizes final PC and CCA truncation points for each predictor. The squared canonical correlations are also listed for each CCA mode in each experiment along with the percentage of the original variance in the predictand explained by each CCA mode. The canonical correlation is the correlation between the predictor and predictand canonical correlation time series for a given CCA mode. Because the squared canonical correlations are the eigenvalues of the cross-correlation matrix, they can be used to calculate the percentage of the original variance in the predictand that is explained by each CCA mode. For example, the first CCA mode (CCA1) from the 13-month leading T200 predictor experiment

TABLE 1. Principal component (PC) and canonical correlation analysis (CCA) truncation points for each experiment. The percentage of the original variance in the predictand and predictor retained after PC truncation and the percentage of the original variance in the predictand explained by each CCA mode are shown in parentheses.

	Truncation points (% var. expl.)			Canonical correlation ² (% predictand var. expl.)			
	PC-Nov.–Dec. SIC	PC-predictor	CCA	CCA1	CCA2	CCA3	CCA4
T200 (preceding October–November)	6 (79)	5 (89)	4	0.68 (40)	0.34 (22)	0.18 (11)	0.11 (6)
V_{sic} (November–December)	6 (79)	4 (84)	4	0.72 (40)	0.51 (29)	0.14 (8)	0.05 (3)

explains 41% of the original variance in the predictand [$79\% \times 0.68(0.68 + 0.34 + 0.18 + 0.11)^{-1}$]. Only 79% of the original variance in the SIC in early winter was used in the CCA analysis because 21% was removed when the number of principal components retained for the analysis was truncated at five (Table 1).

1) T200 EXPERIMENTS (PRECEDING NOVEMBER–DECEMBER)

In the T200 experiment, the CCA was truncated at four, but the modes higher than two explain little of the original variance in the predictand (Table 1). Therefore, it is assumed that the forecast skill of T200 experiments is essentially explained by CCA1. CCA1 represents 40% of the original variance in the sea ice data. The canonical correlation maps and time series for CCA1 are shown in Fig. 8. The positive correlation for the T200 (significant at the 95% confidence level) is found in and around the BSO (Fig. 8a). Conversely, the negative correlation for the SIC (significant at the 95% confidence level) is found in the eastern Barents Sea (Fig. 8b). The signs are opposite between the two fields, suggesting a thermodynamic link. The canonical correlation map for CCA1 shows that significant correlation is also found in the Greenland Sea (Fig. 8a). This result is consistent with the covariability relationship between the time series of the Atlantic water temperature within the Barents Sea (or Greenland Sea) and the upstream NwASC (Skagseth et al. 2008). Because the ocean temperature in these regions approximately corresponds to the oceanic front between the Atlantic and Arctic waters, we suggest that the CCA1 is related to the anomalous Atlantic heat transport.

Because the ocean temperature variation in the BSO leads the SIC variation by 13 months (Fig. 8) and the prediction skill reduces from summer to autumn (Fig. 6), it is expected that warmer ocean temperature set up in the preceding winter in the BSO will be advected along isopycnal surfaces to the Barents Sea within approximately a year and will reemerge to obstruct sea ice formation. To confirm our hypothesis, we examined the lead–lag correlations between the canonical correlation time series for CCA1 and the monthly mean ocean

temperature from the surface to 450-m depth along the zonal section (70° – 73° N), which approximately corresponds to the pathway of the Atlantic water in the Barents Sea. At a lag of -18 months, positive correlations greater than 0.75 appear at 50–200-m depth around the BSO ($\sim 20^{\circ}$ E) (Fig. 9a). At a lag of -12 months, the positive correlations are advected eastward along the isopycnal surface of $27.6\sigma_{\theta}$ (Fig. 9b) and move to 300-m depth along the isopycnal surface of $27.6\sigma_{\theta}$ at a lag of -6 months (Fig. 9c). At no time lag, the positive correlations are found from the surface to 300-m depth (Fig. 9d). These results support the hypothesis that the warmer ocean temperature anomaly in the BSO in the preceding winter affects the sea ice area through the reemergence mechanism.

To diagnose the possibility that ~ 1 -yr lead ocean heat anomaly in the BSO affects the SIC in November–December by winter convection, we examined the climatological advection speed and mixed layer depth in winter. The mixed layer depth is calculated from monthly mean profiles of potential density based on a criterion (a density change from the ocean surface of $0.125\sigma_{\theta}$). Based on the spatial pattern of the subsurface temperature (Fig. 4), the Norwegian Atlantic Current enters the BSO and bifurcates into a northern and southern branch near 25° E. The southern branch turns eastward, rounds the southern side of Sentralbanken, and continues toward the west coast of Novaya Zemlya. The northern branch continues northward. The ocean current at 200-m depth from the NCEP CFSR data shows that the branches have an average current speed of 2 – 3 cm s^{-1} (Fig. 10a). Because the distance between the bifurcation point (25° E) and the sea ice edge (50° E) at 75° N is approximately 700 km, the advection time is approximately 270 to 400 days. In December, the climatological mixed layer depth reaches 200 m near the sea ice edge (Fig. 10b). Thus, the advection time and mixed layer depth are also consistent with the hypothesis that the T200 in the BSO of the preceding October–November affects the November–December SIC in the eastern Barents Sea through the reemergence of the ocean heat content anomaly in the vicinity of the ice edge.

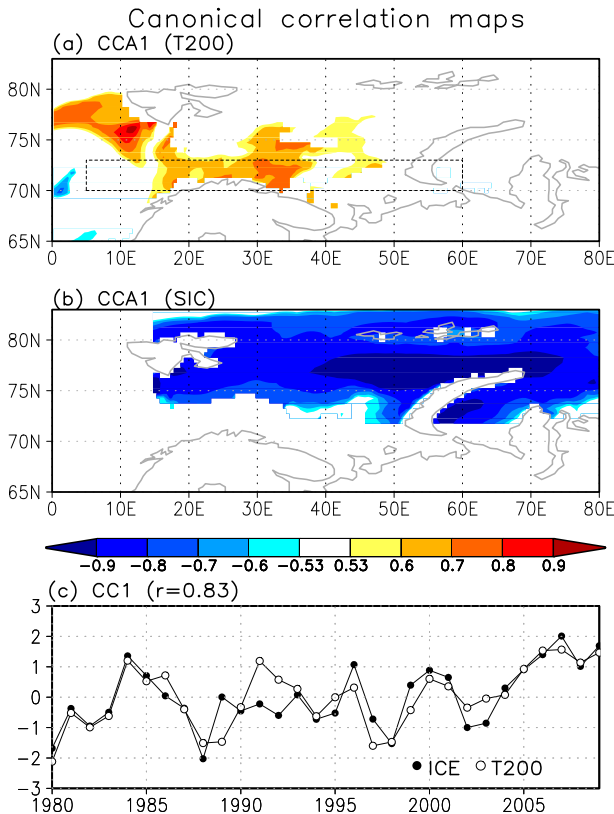


FIG. 8. CCA mode 1 of 1-yr lead T200 predictor experiment: (a) T200 canonical correlation map, (b) November–December sea ice concentration canonical correlation map, and (c) November–December sea ice concentration (closed circles) and T200 (open circles) canonical correlation time series; the canonical correlation $r = 0.83$ (0.77 without linear trend component). Colored regions indicate areas where the correlations are significant at the 95% confidence level.

The canonical correlation time series exhibit decadal fluctuations with positive anomalies in the mid-1980s, 1990s, and 2000s (Fig. 8c). The frequency structure of the relationship between the canonical correlation time series for CCA1 was examined by coherency analysis (von Storch and Zwiers 1999). We calculated the squared coherency, which is equivalent to the correlation between the time series in a frequency domain. The squared coherency is obtained by dividing the squared cross-spectrum between the two time series by their spectra. Before this analysis, we applied zero-padding to both time series data to obtain the low-frequency resolution. The coherency peak significant at the 95% confidence level is evident from 0.1 to 0.2 cycle yr^{-1} ($=5$ to 10 yr) (Fig. 11). This result supports that the covariability between the T200 and SIC is related to the decadal fluctuation. Both time series show the positive trend throughout the analyzed period, which may be related to a recent increase in Atlantic heat transport due to both

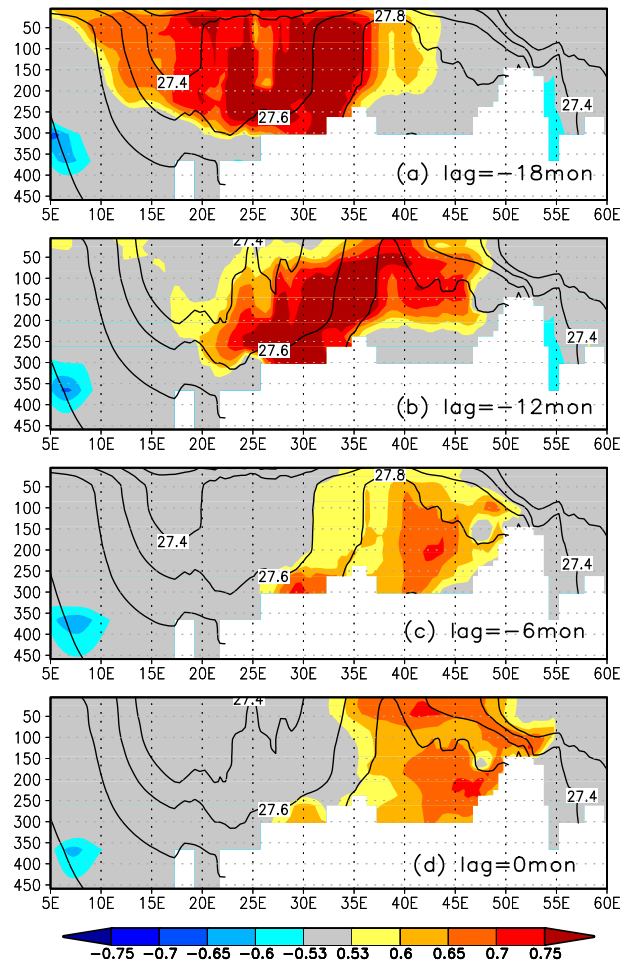


FIG. 9. Lag correlation maps (colors) of 2-monthly mean ocean temperature along the zonal section (70° – 73° N shown in Fig. 8) with T200 canonical correlation time series (CCA1) at lag (a) -18 months to (d) 0 months. The contour lines denote the monthly mean climatological potential density values. Colored regions indicate areas where the correlations are significant at the 95% confidence level.

strengthening and warming of the inflow (Årthun et al. 2012).

Next, to explore the cause of the ocean heat anomaly related to CCA1, we examined the advective effect of the temperature anomaly from the upstream region. Figure 12 shows the lead–lag correlation between the canonical correlation time series for CCA1 and the ocean heat content integrated from 100- to 200-m depth in the North Atlantic. At a lag of -3.5 years, a significant positive correlation appears over the subpolar gyre, indicating that the ocean heat content anomaly leads CCA1. The positive correlation moves northward along the Norwegian shelf break at a lag of -2.5 to -1.5 yr. It then enters the Barents Sea through the BSO and a part of it moves northward to the Greenland Sea. The

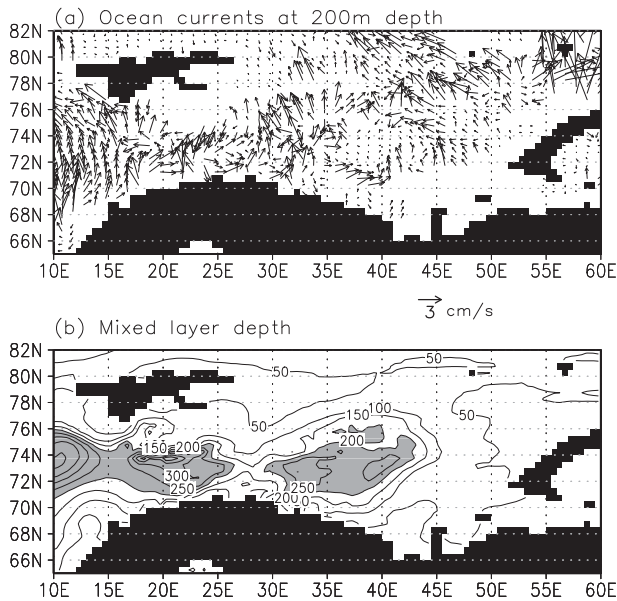


FIG. 10. (a) Annual mean climatology of current vector (cm s^{-1}) at 200-m depth and (b) November–December climatology of mixed layer depth calculated from the NCEP CFSR data. In (b) the regions for the mixed layer depth deeper than 200 m are shaded.

NwASC has an average speed of 5 cm s^{-1} at 100–200-m depth, and the water mass therefore takes 1–2 years to travel from the northeastern Atlantic to the BSO ($\sim 1700 \text{ km}$). This advection time is comparable to the time lag between the ocean heat content in the subpolar gyre and BSO. Conversely, the significant relationship between CCA1 and the local ocean current in the BSO cannot be obtained from the NCEP CFSR data (not shown). Therefore, we conclude that the CCA1 is mostly caused by the ocean heat advection associated with the temperature anomaly from the subpolar gyre.

The above analysis suggests that CCA1 is related to the advection of the ocean heat anomaly from the subpolar gyre. Hátún et al. (2005) suggest that when the subpolar gyre circulation is weakened, the subtropical Atlantic water transport from the northeastern Atlantic to the Nordic seas increases relative to the subpolar water. To confirm that the decadal variability of the ocean heat anomaly in the subpolar gyre can be explained by the subpolar gyre strength, we examined the gyre strength and the associated atmospheric conditions. We used the sea surface height (SSH) data as an indicator of the subpolar gyre strength in accordance with Häkkinen and Rhines (2004). Figure 13a shows the regression map of the 34-month leading December–January SSH against the canonical correlation time series for CCA1. The positive regression of the SSH is found over the subpolar gyre, with a maximum amplitude of 7 cm, indicating that the ocean heat content is negatively correlated with the

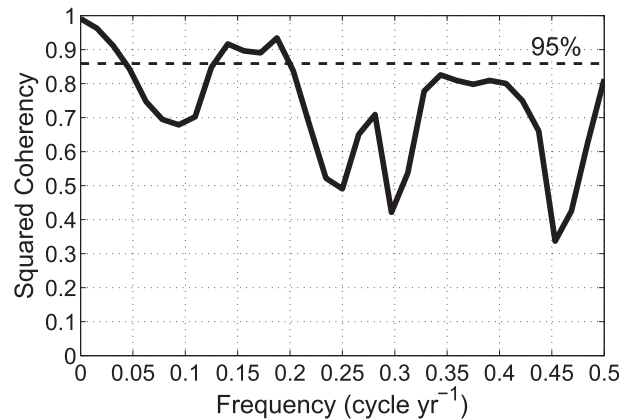


FIG. 11. Squared coherency between T200 and November–December sea ice concentration canonical correlation time series (CCA1). The horizontal dashed lines indicate the confidence levels at 95%.

strength of the subpolar gyre. Moreover, the weakened subpolar gyre is related to the reduced net surface heat flux from the ocean to the atmosphere (Fig. 13b) and weakened Icelandic low (Fig. 13c). The regression pattern of the positive anomaly in the Icelandic low and the negative anomaly in the Azores high is similar to the negative phase of the North Atlantic Oscillation (NAO). This result is consistent with that of Häkkinen and Rhines (2004), who showed that the subpolar gyre is weakened by local air–sea buoyancy forcing related to the negative phase of the NAO. Thus, we suggest that the decadal variability of the ocean heat content in the subpolar gyre responsible for the change in the sea ice area of the Barents Sea is controlled by a ~ 3 -yr leading NAO signal.

2) MERIDIONAL WIND EXPERIMENTS (NOVEMBER–DECEMBER)

In the V_{sfc} experiment, distinct canonical correlations were obtained at the first mode, which represents 40% of the original variance in the sea ice data (Table 1). The canonical correlation maps and time series for the leading CCA mode are shown in Fig. 14. The canonical correlation pattern in CCA1 is characterized by a positive band from Scandinavia over the entire Barents Sea into the Arctic Ocean (Fig. 14a). The opposite sign between V_{sfc} (Fig. 14a) and SIC (Fig. 14b) indicates that the southerly wind anomaly is related to the negative anomaly in the SIC. Because the southerly wind is accompanied by warmer air temperature from the south, V_{sfc} connects to the SIC through thermodynamic processes of turbulent heat flux and dynamical processes associated with the geostrophic wind (Kimura and Wakatsuchi 2001).

The canonical correlation time series of CCA1 exhibits remarkable year-to-year variability (Fig. 14c).

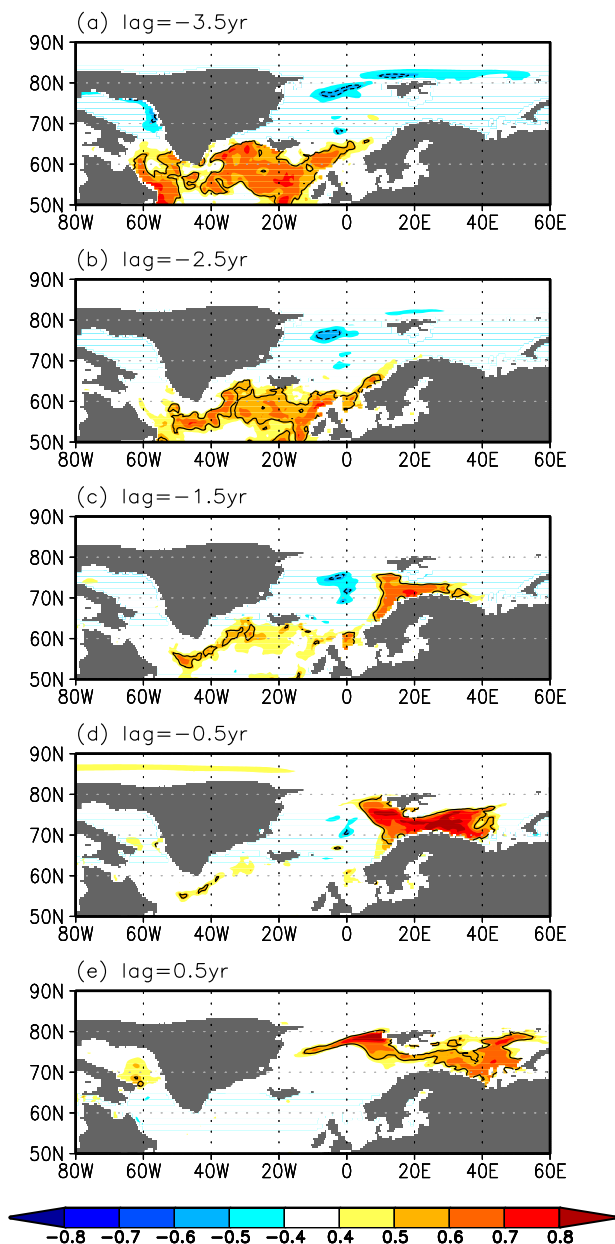


FIG. 12. Lead-lag correlation maps (colors) of the 2-monthly mean ocean heat content (integrated from 100-m to 200-m depth) with T200 canonical correlation time series (CCA mode 1) at lag (a) -3.5 yr to (e) $+0.5$ yr. The contour indicates the region where the absolute value of the correlation is significant at the 95% confidence level.

The canonical correlation time series for CCA1 implies that the southerly wind anomaly is partly related to the reduction of the sea ice area in 1984, and from 2005 to 2009. Thus, we suggest that the remarkable reduction of sea ice area in these years (Fig. 3) is related to the southerly wind anomaly of CCA1.

To understand the atmospheric circulation pattern related to the leading CCA modes of the meridional

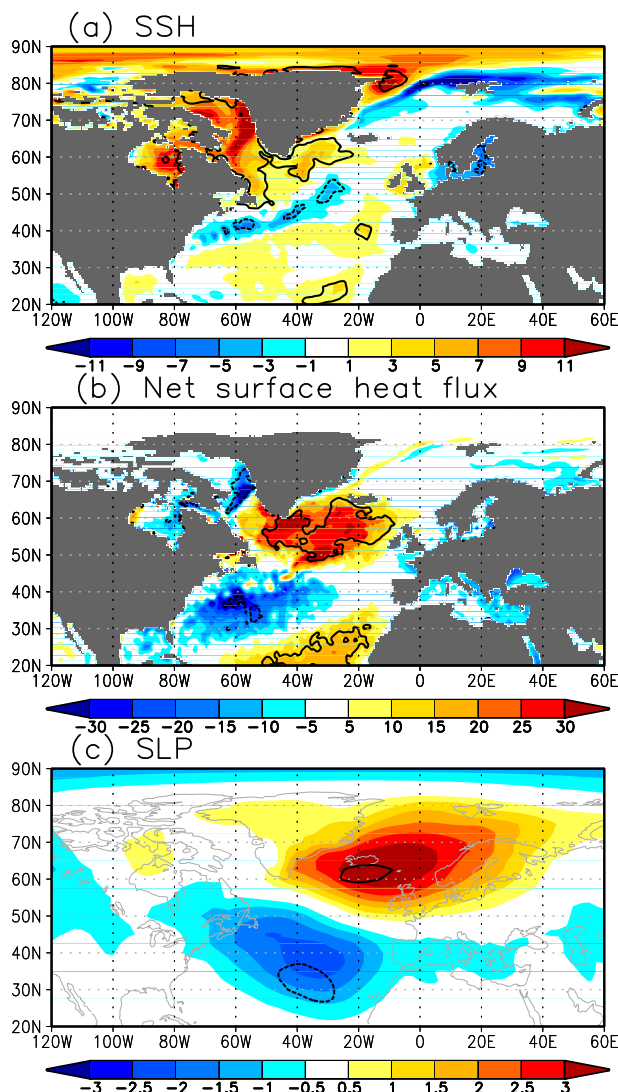


FIG. 13. Regressions (colors) between 34-month leading (December–January) (a) sea surface height (cm), (b) net surface heat flux (W m^{-2}), and (c) sea level pressure (hPa) and T200 canonical correlation time series (CCA mode 1). The positive value in (b) denotes downward flux (heat gain from the atmosphere). The contour indicates areas where the correlation between them exceeds the 95% confidence level.

wind, we performed regression analyses of the geopotential height at 500 hPa ($z500$) in winter (November–December) onto the predictor canonical correlation time series. Figure 15a shows the regression map of $z500$ against the canonical component time series of CCA1. The southerly wind anomaly over the western Barents Sea is related to a positive anomaly over the Barents Sea. Meaningful anomalies of $z500$ are also found over Eurasia and the Greenland Sea showing negative anomalies and the subtropical North Atlantic with a positive value. The wavelike pattern of these anomalies is similar to the

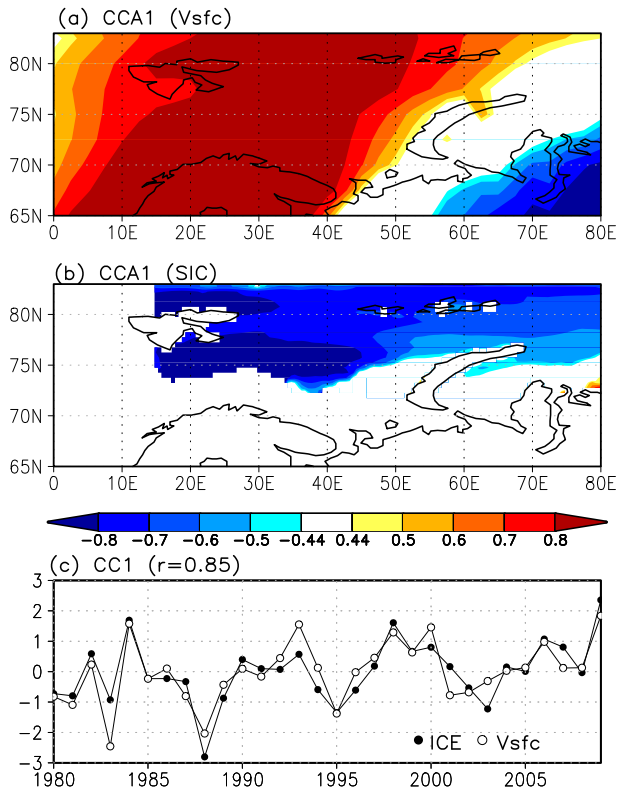


FIG. 14. As in Fig. 8, but for CCA mode 1 of the November–December V_{sfc} predictor experiment. The canonical correlation $r = 0.85$.

spatial pattern of geopotential height in the upper troposphere in the linear baroclinic model (LBM) driven by annual heating in the Gulf Stream (Minobe et al. 2008). The similar response of the upper troposphere can also be found in the LBM driven by the wintertime diabatic heating (Sato et al. 2014).

To confirm that the wavelike patterns over the Northern Hemisphere related to the leading CCA modes are caused by the surface heat flux associated with the Gulf Stream, we examined the SST and the related surface heat flux in the Gulf Stream. Figure 16a shows the regression maps of SST against the canonical component time series of CCA1. The positive regressions are found along the Gulf Stream front, with maximum amplitudes greater than 0.5°C and a significant correlation at the 95% confidence level. To check whether the SST variations along the Gulf Stream front related to the leading CCA modes are apparent one by the local atmospheric variability or not, we examined 1-month leading surface heat fluxes. The regression maps of the net surface heat flux in October–November show the negative values found in the Gulf Stream front (Fig. 16b). The correspondence of positive SST regressions to upward heat flux regressions in this region indicates that local heat fluxes occur from

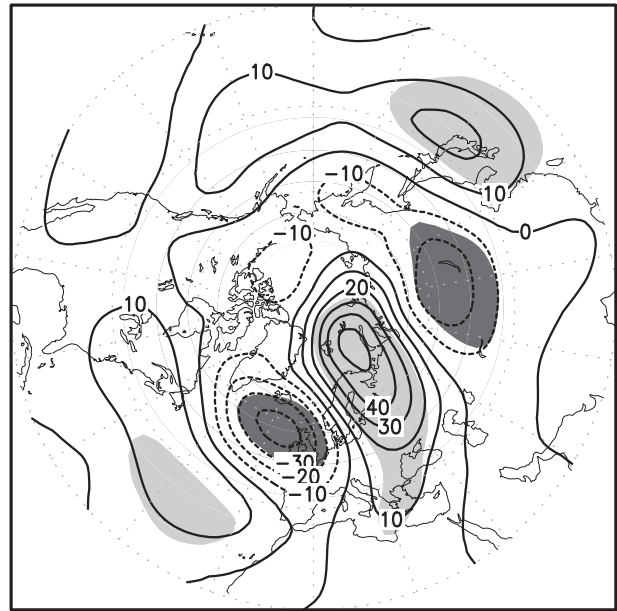


FIG. 15. Regression between November–December 500-hPa geopotential height (m) and V_{sfc} canonical correlation time series for CCA1. Light and dark shading indicates areas where the positive and negative correlation between them exceeds the 95% confidence level, respectively.

the ocean to the atmosphere, and the positive SST regressions (Fig. 16a) are not apparent one by the local atmospheric variability. The regions of significant correlation along the Gulf Stream front are approximately consistent with the centers of action for the atmospheric response to the Gulf Stream front in winter (Minobe et al. 2010). We note that positive regressions in SST are also found over the internal region of the subtropical gyre (Fig. 16a). These positive regressions are related to the ocean response to atmospheric change, because the sign of the regressions for the net surface heat flux is identical to those for the SST (Fig. 16b).

Because our results (Figs. 15 and 16) provide indirect evidence of SST in the Gulf Stream as the driver of the Northern Hemispheric wavelike patterns, we checked the likelihood of this by calculating the correlation maps of z_{500} and SIC onto the Gulf Stream SST in November–December. The Gulf Stream SST is defined by the SST averaged over the area that covers the significant correlations in Fig. 16a (37.5° – 42.5°N , 55° – 70°W). From the regression map of z_{500} (Fig. 17a), we found that the wavelike patterns are similar to those of z_{500} on the V_{sfc} canonical correlation time series for CCA1 (Fig. 15), with positive anomalies over the subtropical North Atlantic and Scandinavia and negative anomalies over Greenland. Furthermore, the Gulf Stream SST is negatively correlated with the November–December SIC in

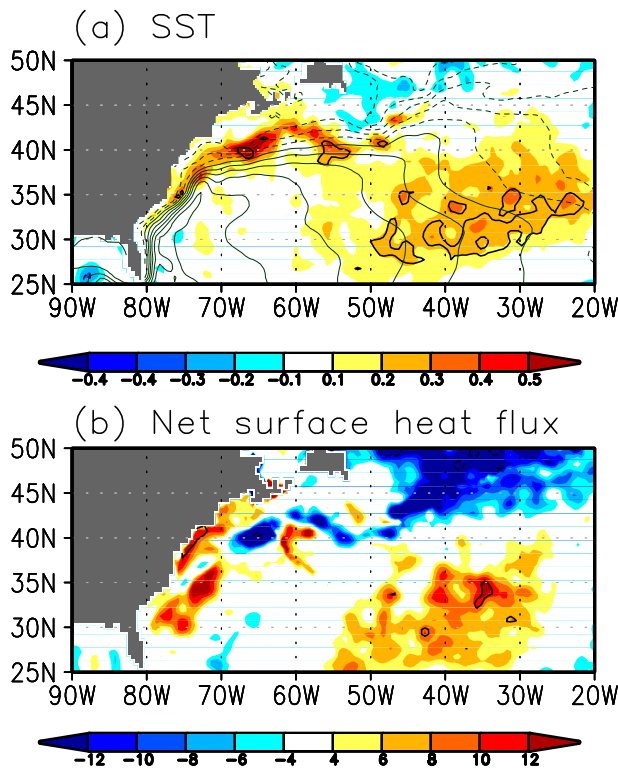


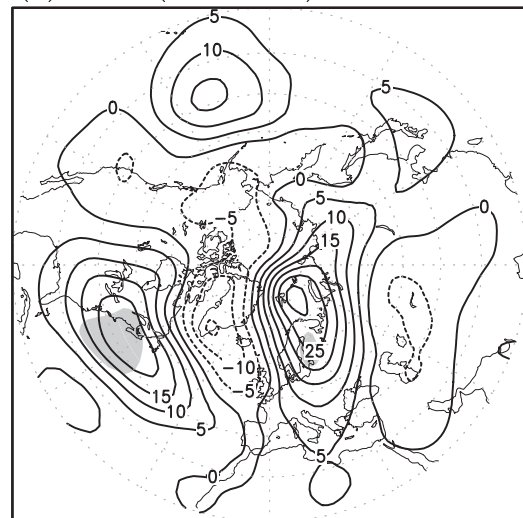
FIG. 16. Regression of (a) November–December SST ($^{\circ}\text{C}$ in color) and (b) October–November net surface heat flux (W m^{-2}) onto V_{sfc} canonical correlation time series for CCA1. The positive values in (b) denote downward flux (heat gain from the atmosphere). The contour indicates areas where the correlation between them exceeds the 95% confidence level. The climatology of the sea surface height (cm in thin green contours) is superimposed.

the western part of the Barents Sea (Fig. 17b). These results support our hypothesis that the SST variation in the Gulf Stream is the driver of Northern Hemispheric wavelike patterns and further affects the sea ice variations in the Barents Sea.

Regarding the cause of the SST variations that governs the waves, it is expected that gyre circulation change leads to the SST anomaly because the SST signal is confined to the Gulf Stream front (Frankignoul et al. 2001). We briefly examined the SST variations in the Gulf Stream and the associated atmospheric conditions. Based on the lag correlation analysis between the SLP and the SST in the Gulf Stream, a significant positive correlation was found over the subtropical North Atlantic, when the former leads the latter by 11 months (Fig. 18). The positive correlation is associated with a negative correlation over the Icelandic low. These regression patterns are similar to the positive phase of the NAO. The leading time of 11 months of the NAO over the SST in the Gulf Stream is consistent with Joyce et al. (2000), who found that the yearly position of the Gulf Stream is highly

Reg. & Cor. maps onto SST in GS (Nov.–Dec.)

(a) z500 (Nov.–Dec.)



(b) SIC (Nov.–Dec.)

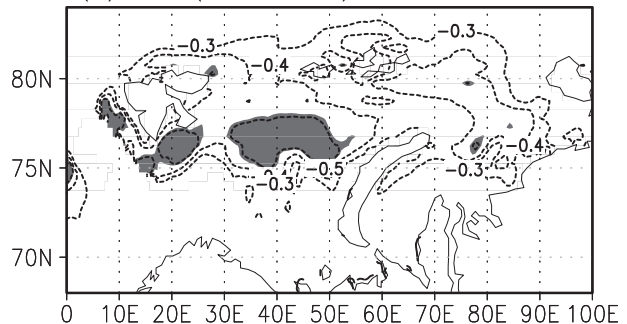


FIG. 17. (a) Regression (contours) between November–December 500-hPa geopotential height and the time series of the SST in the GS front. (b) Correlation (contours) between November–December SICs and the time series of the SST in the GS front. In (a) and (b), light and dark shading indicates areas where the positive and negative correlation between them exceeds the 95% confidence level, respectively.

correlated with the NAO during winter, when the former lags the latter by a year from observations. They suggest that the 1-yr delay is controlled by the potential vorticity of the recirculation gyres. Therefore, such a physical process may be partly related to the SST variations that could govern the waves.

c. Influence of the Barents Sea ice variability on Eurasian winter climate

The CCA diagnostics suggest that the Barents Sea ice area anomalies in early winter are predicted well by the 13-month lead T200 and in-phase V_{sfc} . Because V_{sfc} is related to the wavelike patterns over the North Atlantic, which further extends to the Eurasian continent, it is possible that a severe winter in the Eurasian continent is

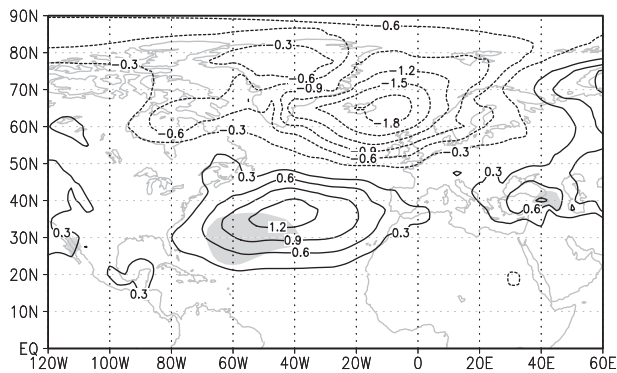


FIG. 18. Regression (hPa) between 11-month leading (December–January) sea level pressure and the time series of November–December SST in the GS front. The zero contour is omitted. Light and dark shading indicate areas where the positive and negative correlation between them exceeds the 90% confidence level, respectively.

caused not only by the atmospheric responses to the Barents Sea ice variation (Honda et al. 2009; Petoukhov and Semenov 2010; Francis and Vavrus, 2012; Inoue et al. 2012) but also by the Gulf Stream front variation in SST. To evaluate the effects of the sea ice variability and the wavelike pattern of the atmosphere on the early winter climate on the Eurasian continent, we calculated the correlation between the canonical component time series of SIC for the leading modes of T200 and V_{sfc} and the winter climate variables (SLP and SAT) on the Eurasian continent in November–December. Although earlier studies discuss the wintertime (January–February) atmospheric response to the autumn sea ice variation (Honda et al. 2009), we focus on the atmospheric response only in November–December because it appears that the air–sea interaction in the sea ice edge as well as the wavelike pattern of the atmosphere affect the downstream climate with no time lag.

The correlation between the canonical component time series of SIC for CCA1 (T200) and CCA1 (V_{sfc}) is 0.56 (significant at the 95% confidence level). The significant correlation relationship is partly related to the recent positive anomalies from 2005 to 2009, which is a common feature in CCA1 (T200) and CCA1 (V_{sfc}) (Figs. 8c and 14c). After subtracting the anomalies in these years, the correlation between CCA1 (T200) and CCA1 (V_{sfc}) from 1980 to 2004 becomes small ($r = 0.44$), and hereafter we use the canonical component time series of SIC and winter climate variables from 1980 to 2004. It is known that the SAT on the Eurasian continent has been dominated by a large positive trend in winter during the past several decades (Serreze and Francis 2006). To evaluate the influence of these CCA modes on the interannual variability of the Eurasian winter climate without the linear trend, we removed the linear trend

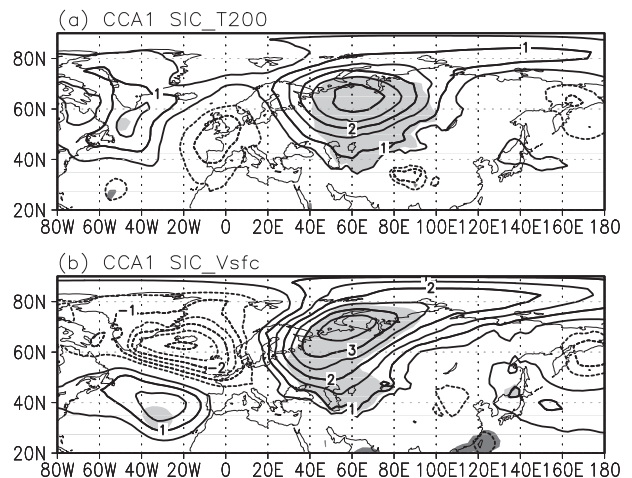


FIG. 19. Regression (hPa) between November–December sea level pressure and sea ice concentration canonical correlation time series of (a) T200 (CCA1) and (b) V_{sfc} (CCA1) from 1980 to 2004. The zero contour is omitted. Light and dark shading indicate areas where the positive and negative correlation between them exceeds the 90% confidence level, respectively.

component from both the SAT data and canonical component time series before the regression analysis for the SAT.

Figure 19 shows the regression maps of the SLP against the canonical component time series of the SIC for the leading mode of T200 and V_{sfc} (the sign of the canonical component time series of the SIC is inverted). Positive regressions, with a maximum amplitude of 4 hPa, are found over the Eurasian continent in each regression map, indicating that the negative SIC anomaly is related to the positive SLP anomaly. The regression maps for the SAT show that negative regression is found over the Eurasian continent, with a maximum amplitude of -1.5°C (Fig. 20). These results suggest that the severe winter conditions on the Eurasian continent may also be induced by an atmospheric response to the Gulf Stream front variation in SST as well as the atmospheric response to the Barents Sea ice variation.

4. Summary and discussion

To examine the predictability of the sea ice variability in the Barents Sea in early winter, we conducted a CCA with atmospheric and ocean anomalies from NCEP CFSR data. We found that the highest prediction skill is obtained from the 13-month lead subsurface temperature at a 200-m depth (T200). The T200 for negative sea ice anomalies exhibit warm anomalies in the subsurface ocean temperature downstream of NwASC. The T200 skillfully predicts SIC variability in 35% of the Barents Sea mainly in the eastern side, and shows decadal

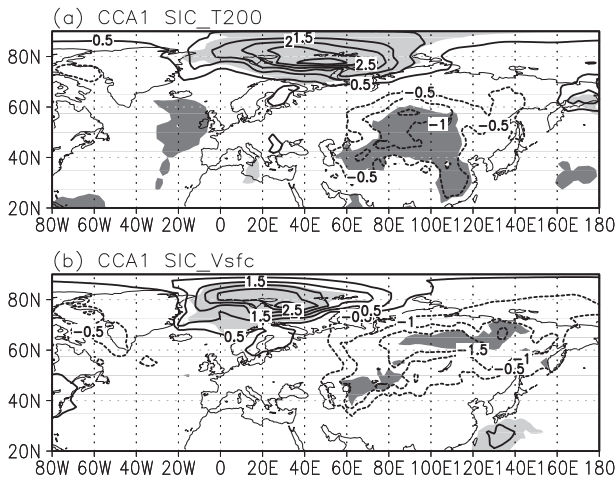


FIG. 20. As in Fig. 19, but for surface air temperature ($^{\circ}\text{C}$) in November–December. The linear trend components are removed from both the SAT data and canonical component time series.

fluctuations with positive anomalies in the mid-1980s, 1990s, and 2000s. The significant correlation between the spring SST near the Barents Sea ice edge and the wintertime sea ice area has been previously reported (Schlichtholz 2011). Additionally, this study indicates that the variability of summer Atlantic water temperature in the BSO is highly correlated with the following winter sea ice area. Our result implies that the prediction skill is further improved using ~ 1 -yr leading T200 rather than the spring SST data and summer subsurface temperature in the BSO. The lead time of T200 is expected to be 4 months longer than that for the spring SST data shown by Schlichtholz (2011). Subsurface temperature data are available in winter from the hydrographic observations by the Institute of Marine Research. If we use the subsurface temperature in January, we can predict the early wintertime SICs 10 months in advance.

The CCA diagnostics reveal that the ocean heat content anomaly in the subpolar North Atlantic gyre precedes the T200 anomaly downstream of the NwASC by approximately 3 years. The ocean heat content is negatively correlated with the strength of the subpolar North Atlantic gyre. This result suggests that the positive (negative) anomaly of the ocean heat content governed by the weakened (strengthened) subpolar North Atlantic gyre leads to warm (cold) water supply to the Barents Sea and results in a decrease (increase) in the Barents Sea ice area on decadal time scales. The influence of the intensity of the subpolar North Atlantic gyre on the heat transport in the North Atlantic Current and Arctic Ocean was shown by Hátún et al. (2005). Our study suggests that the ocean heat condition generated by the subpolar North Atlantic gyre affects the SICs in

the Barents Sea on decadal time scales in a manner similar to the mechanism of the Atlantic water inflow variability.

The lead–lag relationship between the sea ice extent in the Barents Sea and the strength of the Icelandic low related to the NAO was revealed by Sorteberg and Kvingedal (2006). They found that the 1–2-yr lead in cyclone activity over the western Nordic seas strongly influences the Barents Sea ice extent during winter through modulation of the Atlantic water inflow. Their results were also confirmed by a numerical model simulation (Årthun et al. 2012). In this study, we found that a 4-yr lead in heat transport originating from the subpolar gyre is significant for the sea ice area variability. This lead time of the predictor is 2–3 years longer than the previous estimate. Thus, further improvement in sea ice prediction for the Barents Sea is expected based on the 4-yr lead in subpolar gyre strength as well as the change in the rate of volume transport across the BSO.

The CCA also reveals that in-phase V_{sfc} has a forecast skill for the SIC comparable to T200; V_{sfc} skillfully predicts SIC variability in 32% of the Barents Sea, mainly in the western side. The leading modes of CCA exhibit remarkable year-to-year variability with the positive anomalies in 1984, and from 2005 to 2009. The southerly wind anomaly is related to the decrease in the sea ice area. This result implies that the SICs are controlled by the dynamical process associated with the meridional geostrophic wind and the thermodynamic effects associated with air temperature. Because the sea ice area averaged over the Barents Sea in November–December is remarkably small in 1984, we suggest that the effects of V_{sfc} contributed to the decrease in sea ice area during this year.

CCA diagnostics for the meridional wind reveal that the leading CCA modes of V_{sfc} are related to the teleconnection pattern of z500 from the subtropical North Atlantic to the Eurasian continent. This pattern is similar to the spatial pattern of geopotential height in the upper troposphere in the LBM driven by diabatic heating in the Gulf Stream (Minobe et al. 2008). This indicates that the wintertime upward motion over the Gulf Stream can reach the upper troposphere (~ 500 hPa), although the diabatic heating in winter is less than that in summer. In fact, the diabatic heating in the Gulf Stream front in early winter excites the wavelike pattern of geopotential height at 500 hPa over the North Atlantic, which is related to the southerly wind anomaly over the Barents Sea, although the amplitude of the response of the atmosphere is about half or a third of the observed amplitude (Sato et al. 2014). These numerical studies as well as our statistical analysis suggest that the meridional wind responsible for the sea ice variability in November–December is partly

caused by the atmospheric response to the wintertime heat flux in the Gulf Stream front. Further examination is needed to understand the role of the oceanic heat flux in the Gulf Stream front on the large-scale atmospheric pattern over the North Atlantic and the related southerly wind anomaly over the Barents Sea.

The climatological subsurface temperature in the NCEP CFSR has a negative bias compared with the observed data, although the interannual variabilities of the subsurface temperature and SIC in the NCEP CFSR data are comparable to those of the observed data in some sections. This may be related to the fact that the spatial resolution of the ocean model used in the NCEP CFSR is insufficient to represent the narrow structure of the ocean current. Because our study is based on the statistical analysis of the NCEP CFSR data and not on raw observations [in contrast to, e.g., Schlichtholz (2011)], further quantitative study using both observations and numerical simulations is needed to evaluate the remote effects of the ocean heat content and the large-scale atmospheric circulation on the SIC variability.

Seasonal predictability of the Pan-Arctic sea ice extent has previously been examined with a fully coupled global climate model (Chevallier et al. 2013; Wang et al. 2013). The authors suggest that these climate models can skillfully predict the wintertime sea ice extent at a lead time of several months, and the accuracy of the seasonal sea ice prediction highly depends on the initial condition of the sea ice itself. Conversely, because the horizontal grid spacing of the ocean component used in these global climate models is not fine enough to resolve the Gulf Stream front and the narrow current system in and around the Barents Sea (Chassignet and Marshall 2008), there is a possibility that the surface heat flux in the Gulf Stream and lateral advection of the North Atlantic water is not adequately represented. Our study suggests that these ocean thermal conditions make a relatively large contribution to the predictability of the Barents Sea ice in early winter. Therefore, the use of an eddy-resolving ocean model for a climate model may lead to further improvement of the forecast skill of the Pan-Arctic sea ice extent in winter.

Acknowledgments. The hydrographic data in the Kola section were provided by the Polar Research Institute of Marine Fisheries and Oceanography (<http://www.pinro.ru>), Murmansk, Russia. The hydrographic data in the BSO were provided by the Institute of Marine Research (<http://www.imr.no/en>), Bergen, Norway. We wish to thank three anonymous reviewers for their constructive comments. Some figures were produced with the GrADS package developed by B. Doty. This work was

supported by funding from a Grant-in-Aid for Scientific Research (24241009, 22221001), for Scientific Research on Innovative Areas, and for JSPS fellows (13J10583).

REFERENCES

- Årthun, M., and C. Schrum, 2010: Ocean surface heat flux variability in the Barents Sea. *J. Mar. Syst.*, **83**, 88–98, doi:10.1016/j.jmarsys.2010.07.003.
- , T. Eldevik, L. H. Smedsrud, Ø. Skagseth, and R. B. Ingvaldsen, 2012: Qualifying the influence of Atlantic heat on Barents Sea ice variability and retreat. *J. Climate*, **25**, 4736–4743, doi:10.1175/JCLI-D-11-00466.1.
- Barnett, T. P., and R. Preisendorfer, 1987: Origins and levels of monthly and seasonal forecast skill for United States surface air temperatures determined by canonical correlation analysis. *Mon. Wea. Rev.*, **115**, 1825–1850, doi:10.1175/1520-0493(1987)115<1825:OALOMA>2.0.CO;2.
- Barnston, A. G., 1994: Linear statistical short-term climate predictive skill in the Northern Hemisphere. *J. Climate*, **7**, 1513–1564, doi:10.1175/1520-0442(1994)007<1513:LSSTCP>2.0.CO;2.
- Bengtsson, L., and Coauthors, 2007: The need for a dynamical climate reanalysis. *Bull. Amer. Meteor. Soc.*, **88**, 495–501, doi:10.1175/BAMS-88-4-495.
- Blindheim, J., and H. Loeng, 1981: On the variability of Atlantic influence in the Norwegian and Barents Seas. *Fisk. Skr. Ser. Havunder.*, **17**, 161–189.
- Bretherton, C. S., C. Smith, and J. M. Wallace, 1992: An intercomparison of methods for finding coupled patterns in climate data. *J. Climate*, **5**, 541–560, doi:10.1175/1520-0442(1992)005<0541:AIOMFF>2.0.CO;2.
- Cavalieri, D. J., 1994: Sea ice algorithm in NASA Sea Ice Validation Program for the Defense Meteorological Satellite Program Special Sensor Microwave Imager: Final Report. NASA Tech. Memo. 104559, 126 pp.
- , C. Parkinson, P. Gloersen, and H. J. Zwally, 1996: Sea ice concentrations from Nimbus-7 SMMR and DMSP SSM/I passive microwave data. National Snow and Ice Data Center, Boulder, CO, digital media. [Available online at <http://nsidc.org/data/nsidc-0051.html>.]
- Chassignet, E. P., and D. P. Marshall, 2008: Gulf Stream separation in numerical ocean models. *Ocean Modeling in an Eddy Regime*, M. W. Hecht and H. Hasumi, Eds., Amer. Geophys. Union, 39–61.
- Chevallier, M., D. Salas y Mélia, A. Voldoire, M. Déqué, and G. Garric, 2013: Seasonal forecasts of the pan-Arctic sea ice extent using a GCM-based seasonal prediction system. *J. Climate*, **26**, 6092–6104, doi:10.1175/JCLI-D-12-00612.1.
- Cohen, J., and Coauthors, 2014: Recent Arctic amplification and extreme mid-latitude weather. *Nat. Geosci.*, **7**, 627–637, doi:10.1038/ngeo2234.
- Conkright, M. E., and Coauthors, 1999: World Ocean Database 1998: Documentation and quality control version 2.0. National Oceanographic Data Center Internal Rep. 14, 127 pp.
- Deser, C., and H. Teng, 2008: Evolution of Arctic sea ice concentration trends and the role of atmospheric circulation forcing, 1979–2007. *Geophys. Res. Lett.*, **35**, L02504, doi:10.1029/2007GL032023.
- , J. Walsh, and M. Timlin, 2000: Arctic sea ice variability in the context of recent atmospheric circulation trends. *J. Climate*, **13**, 617–633, doi:10.1175/1520-0442(2000)013<0617:ASIVIT>2.0.CO;2.

- Divine, D. D., and C. Dick, 2006: Historical variability of sea ice edge position in the Nordic seas. *J. Geophys. Res.*, **111**, C01001, doi:10.1029/2004JC002851.
- Elsner, J. B., and C. P. Schmertmann, 1994: Assessing forecast skill through cross validation. *Wea. Forecasting*, **9**, 619–624, doi:10.1175/1520-0434(1994)009<0619:AFSTCV>2.0.CO;2.
- Francis, J. A., and E. Hunter, 2007: Drivers of declining sea ice in the Arctic winter: A tale of two seas. *Geophys. Res. Lett.*, **34**, L17503, doi:10.1029/2007GL030995.
- , and S. J. Vavrus, 2012: Evidence linking Arctic amplification to extreme weather in mid-latitudes. *Geophys. Res. Lett.*, **39**, L06801, doi:10.1029/2012GL051000.
- Frankignoul, C., G. de Coëtlogon, T. M. Joyce, and S. Dong, 2001: Gulf Stream variability and ocean–atmosphere interactions. *J. Phys. Oceanogr.*, **31**, 3516–3529, doi:10.1175/1520-0485(2002)031<3516:GSVAOA>2.0.CO;2.
- Grumbine, R. W., 1996: Automated passive microwave sea ice concentration analysis at NCEP. NCEP OMB Tech. Note 120, 13 pp.
- Häkkinen, S., and P. B. Rhines, 2004: Decline of subpolar North Atlantic circulation during the 1990s. *Science*, **304**, 555–559, doi:10.1126/science.1094917.
- Hátún, H., A. B. Sandø, H. Drange, B. Hansen, and H. Valdimarsson, 2005: Influence of the Atlantic subpolar gyre on the thermohaline circulation. *Science*, **309**, 1841–1844, doi:10.1126/science.1114777.
- Hilmer, M., M. Harder, and P. Lemke, 1998: Sea ice transport: A highly variable link between Arctic and North Atlantic. *Geophys. Res. Lett.*, **25**, 3359–3362, doi:10.1029/98GL52360.
- Honda, M., J. Inoue, and S. Yamane, 2009: Influence of low Arctic sea-ice minima on anomalously cold Eurasian winters. *Geophys. Res. Lett.*, **36**, L08707, doi:10.1029/2008GL037079.
- Hughes, S. L., N. P. Holliday, E. Colbourne, V. Ozhigin, H. Valdimarsson, S. Østerhus, and K. Wiltshire, 2009: Comparison of in situ time series of temperature with gridded sea surface temperature datasets in the North Atlantic. *ICES J. Mar. Sci.*, **66**, 1467–1479, doi:10.1093/icesjms/fsp041.
- Inoue, J., M. Hori, and K. Takaya, 2012: The role of Barents Sea ice in the wintertime cyclone track and emergence of a warm-Arctic cold-Siberian anomaly. *J. Climate*, **25**, 2561–2568, doi:10.1175/JCLI-D-11-00449.1.
- Joyce, T. M., C. Deser, and M. A. Spall, 2000: The relation between decadal variability of subtropical mode water and the North Atlantic Oscillation. *J. Climate*, **13**, 2550–2569, doi:10.1175/1520-0442(2000)013<2550:TRBDVO>2.0.CO;2.
- Kaplan, D., and L. Glass, 1995: *Understanding Nonlinear Dynamics*. Springer-Verlag, 420 pp.
- Kauker, F., R. Gerdes, M. Karcher, C. Köberle, and J. L. Lieser, 2003: Variability of Arctic and North Atlantic sea ice: A combined analysis of model results and observations from 1978 to 2001. *J. Geophys. Res.*, **108**, 3182, doi:10.1029/2002JC001573.
- Kimura, N., and M. Wakatsuchi, 2001: Mechanisms for the variation of sea ice extent in the Northern Hemisphere. *J. Geophys. Res.*, **106** (C12), 31 319–31 331, doi:10.1029/2000JC000739.
- Koenigk, T., and L. Brodeau, 2014: Ocean heat transport into the Arctic in the twentieth and twenty-first century in EC-Earth. *Climate Dyn.*, **42**, 3101–3120, doi:10.1007/s00382-013-1821-x.
- , U. Mikolajewicz, J. H. Jungclaus, and A. Kroll, 2009: Sea ice in the Barents Sea: Seasonal to interannual variability and climate feedbacks in a global coupled model. *Climate Dyn.*, **32**, 1119–1138, doi:10.1007/s00382-008-0450-2.
- Kwok, R., 2009: Outflow of Arctic Ocean sea ice into the Greenland and Barents Seas: 1979–2007. *J. Climate*, **22**, 2438–2457, doi:10.1175/2008JCLI2819.1.
- Livezey, R. E., and T. M. Smith, 1999: Considerations for use of the Barnett and Preisendorfer (1987) algorithm for canonical correlation analysis of climate variations. *J. Climate*, **12**, 303–305, doi:10.1175/1520-0442-12.1.303.
- Maslanik, J., S. Drobot, C. Fowler, W. Emery, and R. Barry, 2007: On the Arctic climate paradox and the continuing role of atmospheric circulation in affecting sea ice conditions. *Geophys. Res. Lett.*, **34**, L03711, doi:10.1029/2006GL028269.
- Michaelsen, J., 1987: Cross-validation in statistical climate forecast models. *J. Climate Appl. Meteor.*, **26**, 1589–1600, doi:10.1175/1520-0450(1987)026<1589:CVISCF>2.0.CO;2.
- Minobe, S., A. Kuwano-Yoshida, N. Komori, S.-P. Xie, and R. J. Small, 2008: Influence of the Gulf Stream on the troposphere. *Nature*, **452**, 206–209, doi:10.1038/nature06690.
- , M. Miyashita, A. Kuwano-Yoshida, H. Tokinaga, and S.-P. Xie, 2010: Atmospheric response to the Gulf Stream: Seasonal variations. *J. Climate*, **23**, 3699–3719, doi:10.1175/2010JCLI3359.1.
- O’Lenic, E. A., and R. E. Livezey, 1988: Practical considerations in the use of rotated principal component analysis (RPCA) in diagnostic studies of upper-air height fields. *Mon. Wea. Rev.*, **116**, 1682–1689, doi:10.1175/1520-0493(1988)116<1682:PCITUO>2.0.CO;2.
- Parkinson, C. L., and D. J. Cavalieri, 2008: Arctic sea ice variability and trends, 1979–2006. *J. Geophys. Res.*, **113**, C07003, doi:10.1029/2007JC004558.
- Peings, Y., and G. Magnusdottir, 2014: Response of the wintertime Northern Hemisphere atmospheric circulation to current and projected Arctic sea ice decline: A numerical study with CAM5. *J. Climate*, **27**, 244–264, doi:10.1175/JCLI-D-13-00272.1.
- Petoukhov, V., and V. A. Semenov, 2010: A link between reduced Barents–Kara Sea ice and cold winter extremes over northern continents. *J. Geophys. Res.*, **115**, D21111, doi:10.1029/2009JD013568.
- Polyakov, I. V., and Coauthors, 2005: One more step toward a warmer Arctic. *Geophys. Res. Lett.*, **32**, L17605, doi:10.1029/2005GL023740.
- Rayner, N. A., D. E. Parker, E. B. Horton, C. K. Folland, L. V. Alexander, D. P. Rowell, E. C. Kent, and A. Kaplan, 2003: Global analyses of sea surface temperature, sea ice, and night marine air temperature since the late nineteenth century. *J. Geophys. Res.*, **108**, 4407, doi:10.1029/2002JD002670.
- Roemmich, D., and Coauthors, 2001: The global array of profiling floats. *Observing the Ocean in the 21st Century*, C. J. Koblinsky and N. R. Smith, Eds., Australian Bureau of Meteorology, 248–258.
- Saha, S., and Coauthors, 2010: The NCEP Climate Forecast System Reanalysis. *Bull. Amer. Meteor. Soc.*, **91**, 1015–1057, doi:10.1175/2010BAMS3001.1.
- Sandø, A. B., J. E. Ø. Nilsen, Y. Gao, and K. Lohmann, 2010: Importance of heat transport and local air–sea heat fluxes for Barents Sea climate variability. *J. Geophys. Res.*, **115**, C07013, doi:10.1029/2009JC005884.
- Sato, K., J. Inoue, and M. Watanabe, 2014: Influence of the Gulf Stream on the Barents Sea ice retreat and Eurasian coldness during early winter. *Environ. Res. Lett.*, **9**, 084009, doi:10.1088/1748-9326/9/8/084009.
- Schlichtholz, P., 2011: Influence of oceanic heat variability on sea ice anomalies in the Nordic Seas. *Geophys. Res. Lett.*, **38**, L05705, doi:10.1029/2010GL045894.

- , 2013: Observational evidence for oceanic forcing of atmospheric variability in the Nordic seas area. *J. Climate*, **26**, 2957–2975, doi:10.1175/JCLI-D-11-00594.1.
- , and M.-N. Houssais, 2011: Forcing of oceanic heat anomalies by air–sea interactions in the Nordic seas area. *J. Geophys. Res.*, **116**, C01006, doi:10.1029/2009JC005944.
- Screen, J. A., 2014: Arctic amplification decreases temperature variance in northern mid- to high-latitudes. *Nat. Climate Change*, **4**, 577–582, doi:10.1038/nclimate2268.
- , and I. Simmonds, 2014: Amplified mid-latitude planetary waves favour particular regional weather extremes. *Nat. Climate Change*, **4**, 704–709, doi:10.1038/nclimate2271.
- Serreze, M. C., and J. A. Francis, 2006: The Arctic amplification debate. *Climatic Change*, **76**, 241–264, doi:10.1007/s10584-005-9017-y.
- , A. Barrett, A. Slater, M. Steele, J. Zhang, and K. Trenberth, 2007: The large-scale energy budget of the Arctic. *J. Geophys. Res.*, **112**, D11122, doi:10.1029/2006JD008230.
- Shapiro, I., R. Colony, and T. Vinje, 2003: April sea ice extent in the Barents Sea, 1850–2001. *Polar Res.*, **22**, 5–10, doi:10.1111/j.1751-8369.2003.tb00089.x.
- Simmonds, I., and K. Keay, 2009: Extraordinary September Arctic sea ice reductions and their relationships with storm behavior over 1979–2008. *Geophys. Res. Lett.*, **36**, L19715, doi:10.1029/2009GL039810.
- Simonsen, K., and P. M. Haugan, 1996: Heat budgets of the Arctic Mediterranean and sea surface heat flux parameterizations for the Nordic seas. *J. Geophys. Res.*, **101**, 6553–6576, doi:10.1029/95JC03305.
- Skagseth, Ø., T. Furevik, R. Ingvaldsen, H. Loeng, K. A. Mork, K. A. Orvik, and V. Ozhigin, 2008: Volume and heat transports to the Arctic Ocean via the Norwegian and Barents Seas. *Arctic Subarctic Ocean Fluxes: Defining the Role of the Northern Seas in Climate*, R. Dickson, J. Meincke, and P. Rhines, Eds., Springer, 45–64.
- Smedsrud, L. H., and Coauthors, 2013: The role of the Barents Sea in the Arctic climate system. *Rev. Geophys.*, **51**, 415–449, doi:10.1002/rog.20017.
- Sorteberg, A., and B. Kvingedal, 2006: Atmospheric forcing on the Barents Sea winter ice extent. *J. Climate*, **19**, 4772–4784, doi:10.1175/JCLI3885.1.
- Tivy, A., S. E. L. Howell, B. Alt, J. J. Yackel, and T. Carrieres, 2011: Origins and levels of seasonal forecast skill for sea ice in Hudson Bay using canonical correlation analysis. *J. Climate*, **24**, 1378–1395, doi:10.1175/2010JCLI3527.1.
- Vihma, T., 2014: Effects of Arctic sea ice decline on weather and climate: A review. *Surv. Geophys.*, **35**, 1175–1214, doi:10.1007/s10712-014-9284-0.
- Vinje, T., 2001: Anomalies and trends of sea-ice extent and atmospheric circulation in the Nordic seas during the period 1864–1998. *J. Climate*, **14**, 255–267, doi:10.1175/1520-0442(2001)014<0255:AATOSI>2.0.CO;2.
- von Storch, H., and F. W. Zwiers, 1999: *Statistical Analysis in Climate Research*. Cambridge University Press, 484 pp.
- Wallace, J. M., and D. S. Gutzler, 1981: Teleconnections in the geopotential height field during the Northern Hemisphere winter. *Mon. Wea. Rev.*, **109**, 784–812, doi:10.1175/1520-0493(1981)109<0784:TITGHF>2.0.CO;2.
- Wang, W., P. Xie, S.-H. Yoo, Y. Xue, A. Kumar, and X. Wu, 2011: An assessment of the surface climate in the NCEP climate forecast system reanalysis. *Climate Dyn.*, **37**, 1601–1620, doi:10.1007/s00382-010-0935-7.
- , M. Chen, and A. Kumar, 2013: Seasonal prediction of Arctic sea ice extent from a coupled dynamical forecast system. *J. Climate*, **141**, 1375–1394, doi:10.1175/MWR-D-12-00057.1.
- Xue, Y., B. Huang, Z.-Z. Hu, A. Kumar, C. Wen, D. Behringer, and S. Nadiga, 2011: An assessment of oceanic variability in the NCEP Climate Forecast System Reanalysis. *Climate Dyn.*, **37**, 2511–2539, doi:10.1007/s00382-010-0954-4.
- Yang, S., and J. H. Christensen, 2012: Arctic sea ice reduction and European cold winters in CMIP5 climate change experiments. *Geophys. Res. Lett.*, **39**, L20707, doi:10.1029/2012GL053338.
- Zhang, X., A. Sorteberg, J. Zhang, R. Gerdes, and J. C. Comiso, 2008: Recent radical shifts of atmospheric circulations and rapid changes in Arctic climate system. *Geophys. Res. Lett.*, **35**, L22701, doi:10.1029/2008GL035607.
- Zwiers, F. W., and H. von Storch, 2004: On the role of statistics in climate research. *Int. J. Climatol.*, **24**, 665–680, doi:10.1002/joc.1027.